Experimental Investigation of Overflow on the Lee Side of River Groins due to Long-Period Primary Ship-Induced Waves Using Particle Image Velocimetry Analysis

Alyousif, Ahmad; Van Batenburg, Tobias; Memar, Sargol; Melling, G.; Hofland, B.

DOI
10.1061/JWPED5.WWENG-2185

Publication date
2025

Document Version
Final published version

Published in
Journal of Waterway, Port, Coastal and Ocean Engineering

Citation (APA)
Alyousif, A., Van Batenburg, T., Memar, S., Melling, G., & Hofland, B. (2025). Experimental Investigation of Overflow on the Lee Side of River Groins due to Long-Period Primary Ship-Induced Waves Using Particle Image Velocimetry Analysis. *Journal of Waterway, Port, Coastal and Ocean Engineering*, *151*(3), Article 04025004. https://doi.org/10.1061/JWPED5.WWENG-2185

Experimental Investigation of Overflow on the Lee Side of River Groins due to Long-Period Primary Ship-Induced Waves Using Particle Image Velocimetry Analysis

Ahmad AlYousif, Ph.D., P.E., M.ASCE[1]; Tobias van Batenburg[2]; Sargol Memar, Ph.D.[3]; G. Melling, Ph.D.[4]; and B. Hofland, Ph.D.[5]

Abstract: The passage of ships in confined waterways creates a stern wave that can overflow bank protection structures such as groins. This overflow, due to the long-period primary ship-induced waves, can be high in velocity, especially at the lee-side slope of groins, potentially causing significant damage to the structure. This study derives an equation to express overflow velocities, intended as a design tool for groins exposed to these types of waves. A detailed experimental investigation was performed on four physical models of groins with different slopes and stone sizes in the armor layer under the influence of different hydraulic heads. Particle image velocimetry (PIV) was used to measure the flow velocities at the crest and lee sides of the structure. All PIV measurements were performed thrice under free-flow conditions with no initial water level at the lee side of the structure. The depth- and time-averaged flow velocities (U_{avg}) were extracted from four positions along the lee-side slope and accelerated from 0.7 to 2.2 m/s. A dimensionless equation of the overflow velocities was obtained as a function of the hydraulic head (h), slope (θ), freeboard (R_c), and nominal rock diameter (d_{n50}). **DOI: 10.1061/JWPED5.WWENG-2185**. *This work is made available under the terms of the Creative Commons Attribution 4.0 International license, https://creativecommons.org/licenses/by/4.0/.*

Author keywords: Primary ship-induced waves; Flow velocity equations; River groins; Particle image velocimetry analysis; Estuarine protection structures; Physical modeling.

Introduction and Literature Review

River groins are manufactured structures that protect riverbanks from erosion, maintain the water level by deflecting the flow direction, and ensure navigational safety (Uijttewaal 2005; Ahmad et al. 2010; Xiang et al. 2020). They are constructed perpendicular to the riverbank and can be composed of rock, concrete, or wood. River groins are usually subjected to loads owing to the flow velocities around the structure or small waves. These loads create drag forces that can erode riverbeds and riverbanks. Installing groins perpendicular to the flow direction decreases the cross section of the water body and reduces the flow velocities behind the structure. Moreover, these structures maintain the main flow of the river at a distance from the bank, which helps reduce erosion at the riverbanks (Prasad et al. 2016). Consequently, the flow velocity and erosion rates increased in the middle of the river, deepening the channel. Therefore, groins are also used to control the depth of navigational channels (Malik and Pal 2019).

A ship wave system consists of primary and secondary waves (Bertram 2012). This system results from a ship displacing water as it moves forward (Bhowmik et al. 1981). The primary wave system includes a bow wave in front of the ship, a stern wave behind it, and a drawdown along the ship between them. A study performed by the German Federal Waterways Engineering and Research Institute (BAW 2010) to improve the design of bank protection structures in German estuaries revealed that primary waves caused by vessel displacements are responsible for rapid groin and training wall deterioration. The mechanism is described in detail by Melling et al. (2021) and involves high-velocity turbulent overflowing of groins that can cause damage to the crest and lee sides of the structures. One hot spot of this type of damage is located in the Elbe estuary, which connects the Port of Hamburg to the North Sea. This waterway is heavily used by ultra large container vessels, such as the New Panamax and Triple E categories. These vessels were brought into service close to 20 years ago; with possible further increases in the future, further damage to bank-side infrastructure is expected. Different engineering measures have been adopted to mitigate the damage caused by the primary ship-induced waves on groins. These measures include the construction of different prototypes with shallower slope angles, smaller crest widths, wider groin root areas, and smoother revetment transitions (WSACux 2009; WSABhv 2021). Based on these experiences, a prototype study was carried out that saw two severely damaged groins in

[1]Assistant Professor, Civil Engineering Dept., Kuwait Univ., P.O. Box 5969, Safat 13060, Kuwait; Visiting Scholar, Faculty of Civil Engineering and Geosciences, Delft Univ. of Technology, Stevinweg 1, Delft 2628 CN, Netherlands (corresponding author). ORCID: https://orcid.org/0000-0002-0428-9839. Email: ahmad.alyousif@ku.edu.kw

[2]M.Sc., Hydraulic Engineer, Dept. of Hydraulics for Infrastructure and Industry, Deltares, Boussinesqweg 1, 2629 HV Delft, The Netherlands. ORCID: https://orcid.org/0009-0004-4055-8110. Email: tobias.vanbatenburg@deltares.nl

[3]Coastal Engineer, Department of Engineering and Estimating, Van Oord Dredging and Marine Contractors, Schaardijk 211, 3063 NH Rotterdam, The Netherlands. ORCID: https://orcid.org/0000-0003-2980-5067. Email: sargol.memar@vanoord.com

[4]Coastal Engineer, Federal Waterways Engineering and Research Institute (BAW), Dept. of Coastal Engineering, Wedeler Landstr 157, 22559 Hamburg, Germany. ORCID: https://orcid.org/0000-0003-2754-0341. Email: gregor.melling@baw.de

[5]Associate Professor, Faculty of Civil Engineering and Geosciences, Delft Univ. of Technology, Stevinweg 1, Delft 2628 CN, Netherlands. ORCID: https://orcid.org/0000-0003-1643-6469. Email: b.hofland@tudelft.nl

Note. This manuscript was submitted on June 18, 2024; approved on December 2, 2024; published online on January 27, 2025. Discussion period open until June 27, 2025; separate discussions must be submitted for individual papers. This paper is part of the ***Journal of Waterway, Port, Coastal, and Ocean Engineering***, © ASCE, ISSN 0733-950X.

the Lower Elbe Estuary being rebuilt with innovative designs (Melling et al. 2021). The responses of the prototypes to ship-induced loading were monitored and assessed. Although one prototype remained stable, the design was based on engineering experience as no actual design tools, whether probabilistic or deterministic, were, at the time, available for designing groins against overflowing primary shipping-induced waves. This has now been remedied, in part, by the design method developed in Seemann et al. (2023); however, there remains uncertainty in the expected flow velocity on the lee side of groins, which is to be addressed in this study. Seemann et al. (2023) predicted the overflow velocity along a slope length (L_s) smaller than that of a fully developed flow length (L_d) using an equation in which the ratio of L_s and L_d was calculated via linear interpolation. However, this method was not validated due to lack of measurements. As reported by Melling et al. (2021), pressure and acoustic-Doppler-velocimeter (ADV) sensors were installed at the head, foot, and crest of the groins during field measurements. However, no sensors were installed on the lee side of the groins; hence, the flow velocities and water levels at this location on the groin were unknown.

The groins in question comprise an armor layer of loose rock. The underlying old structures are thought to have a core that is relatively impermeable. Hence, the overflow behaves similarly to flow over a weir-type structure as shown by Seemann et al. (2023). For the long-period primary wave, the flow can also be approximated as stationary. Weir structures are generally divided into sharp- and finite-crested weirs. They are constructed to control the upstream water levels by changing the flow in the waterways. The discharge depends mainly on the upstream and downstream water levels for finite-crested weirs. As the water approaches the weir structure, the flow starts to accelerate, and the streamlines converge until they reach the crest. At this point, the flow velocity increases and approaches the critical flow condition. Moreover, the streamlines become parallel, causing a decrease in the water level at the crest. The critical flow condition could be satisfied at the crest, for low downstream water level. If the downstream water level is significantly lower than the crest, the flow at the lee-side slope can become critical or even supercritical until it interacts with the downstream water levels. This condition is also known as the free-flow condition, at which the weir discharge can be estimated, as presented by Poleni (1717), and depends on the geometry of the structure and hydraulic conditions. Although this approach provides initial insights into the flow conditions on the slope, the flow velocities remain unclear. Kindsvater (1964) and Fritz and Hager (1998) performed physical modeling experiments for embankments and trapezoidal weir structures. However, the velocity equations were determined at the crest and behind the structure and not at the downward slope. Biabani et al. (2022) performed an experimental investigation in which the flow velocity was measured at the crest and bottom of different gabion weir configurations. However, no velocity equations have yet been presented. Other studies on weirs have focused on determining discharge coefficients. The available literature shows that only a few studies have been conducted to derive velocity equations for sloping structures. Cheng and Gulliver (2011) performed a study in which a model based on the log-wake law was developed to determine the flow velocities along the slope of a stepped spillway. This numerical approach describes the turbulent flow along a downward slope but depends on several assumptions and structure-dependent constants. Owing to the lack of studies on the flow velocity equation along a downward rocky slope, the theoretical maximum mean flow velocity was determined by assuming the developed flow conditions for slopes of large lengths. Therefore, the Manning formula with the Strickler coefficient for riprap is used to determine the theoretical depth- and time-averaged velocities for a fully developed flow (i.e., uniform steady flow, where the flow no longer accelerates) as follows:

$$u_{\text{dev}} = k_s \times R_h^{\frac{2}{3}} \times \theta^{\frac{1}{2}} \tag{1}$$

where u_{dev} = mean of theoretically developed flow velocity along the slope; R_h = hydraulic radius; and θ = slope. The Strickler coefficient (k_s) was calculated as $k_s = b_1/k^{b_2}$, where $k = \theta \times d_{50}$; $b_1 = 12.21$; and $b_2 = 0.159$ for the crushed dumped rocks (Abt et al. 1987).

In the aforementioned literature, knowledge gaps were identified. The main objective of the present study was to measure the overflow velocities at the lee side of a groin subjected to different hydraulic conditions (i.e., representing long-period primary ship-induced wave loadings) via physical modeling. The physical models were designed based on a prototype groin located in the Lower Elbe Estuary, where no significant damage was observed. However, different parameters were varied to obtain a general flow velocity equation under free-flow conditions for the groins. The study is limited to a two-dimensional cross section, with an impermeable core as in the prototype and glued armor and filter layers to maintain the model dimensions throughout the experiment. The overflow due to long-period primary ship-induced waves was approximated using a quasi-steady approximation with no initial downstream water level to obtain supercritical conditions. These experiments were conducted at the Hydraulic Engineering Laboratory at Delft University of Technology, Netherlands. Particle image velocimetry (PIV) was used to measure the overflow velocities. This method is an optical measurement technique in which the velocity field of an entire region within a flow is simultaneously observed by measuring the displacement of particles assumed to follow the flow (Atkins 2016). The main advantage of PIV measurements over traditional point-measurement devices is that PIV is a quantitative flow field mapping technique that can provide insights into the flow behavior of an entire region. PIV is a nonintrusive technique that works by illuminating small seeding particles. Therefore, a PIV system was used in this study to provide more comprehensive results than a point-measurement device. Another reason for not using an initial downstream water level is to maintain a flat-water surface during the PIV measurements of overflow and allow sufficient and consistent light penetration of water.

The obtained overflow velocity equation on the lee side of river groins based on a deterministic tool (i.e., physical modeling results) will help engineers improve the design of such bank protection structures against damage associated with long-period primary ship-induced waves. This equation applies to river groins in the navigational channel of the Lower Elbe Estuary in Germany and other locations with similar conditions.

The remainder of this paper is organized as follows: Details of the research methodology and physical modeling experiment are provided in the second section. The results and discussion are presented in the third section. The main conclusions, recommendations, and limitations of the study are presented in the last section.

Methodology

Froude scaling of configuration and flow was applied as well as a fixed and rough bed (Hughes 1993; Chanson 2004). This section provides details of the experimental description, dimensional and dimensionless flow equations, prototype and tested models, PIV experimental setup, and flow velocity analysis.

Testing Facility and Experimental Description

A tilted flume, which is 14.3 m in length and 0.4 m in width and height, is used to test the performance of tested models under different hydraulic conditions (Fig. 1). The flume consisted of an experimental flume and a return flume. All models were fixed at 7.15 m from the inlet. An inlet valve was used to manually control the inlet flow using water from the central basin of the laboratory. The water level inside the flume was controlled manually using a movable weir at the downstream end of the flume. The water that flowed over the weir entered the return flume and then returned to the central basin of the laboratory.

The overflow due to long-period primary ship-induced waves can be approximated using a quasi-steady approximation, owing to their long wave period characteristics at shallow water depths. Although the flow is unsteady throughout the primary wave period, the variations are insignificant within a short time step. Therefore, the inertial force within the wave is minimal. As shown by Melling et al. (2021), the prototype has a flow velocity at the crest of 3 m/s, a primary ship wave period of 60–120 s, and a groin width of 19 m, resulting in a Keulegan–Carpenter number (KC) reaching up to 19. KC values become even larger for nominal rock diameters varying from 0.17 to 0.23 m and water depths varying from 3 to 4.41 m. Larger KC values are associated with drag-dominated regimes (Keulegan and Carpenter 1958). Additionally, fully developed flow (i.e., uniform steady flow) is commonly observed at KC >7 (van Steijn et al. 2023). Consequently, the flow instantly adjusts to the upstream and downstream boundary conditions. As a result, the maximum flow velocities in an overflowing wave are approximately equivalent to the flow velocities of a constant water level at the same height as that of a long-period wave. These maximum velocities are expected to cause the most damage; therefore, it is essential to understand them. Moreover, the experiment recreated the maximum flow velocities via free-flow conditions and a fixed water level on the wave-facing side, mimicking those of overflowing primary ship-induced waves with the same wave height. No initial water level at the lee side was present to maintain the flat-water surface of the overflow. This is necessary for PIV measurements to allow the light source to penetrate the water. Furthermore, the lack of an initial water level creates supercritical conditions representing the most extreme overflow conditions. This condition is a conservative but safer approximation for the stability of the structure. Seemann et al. (2023) also obtained a good fit for the prototype's field data when considering the overflow as quasi-stationary. A schematic of the wave-structure interaction is presented in Fig. 2, and a description of the main parameters related to the overflow of long-period primary ship-induced waves on the lee side of a groin is provided in the Notation list. The details of the prototype and tested models, along with the hydraulic conditions, are provided in Sections "Prototype Dimensions and Hydraulic Conditions" and "Tested Physical Models and Experiment Flow Conditions," respectively.

Dimensional and Dimensionless Flow Equations

As noted in the literature review, the flow velocity on the lee side of the groin is only described analytically via the theoretical maximum developed flow velocities based on the Manning equation [Eq. (1)]. This equation can be used for slopes of large lengths; however, it is not expected that the flow over the groins will reach a fully developed state (as verified in Section "Developed Flow Velocity"). Therefore, two equations are derived for the flow on the lee side of the groin: one based on the Bernoulli equation (Section 'Dimensional Flow Equation") and the other using a dimensional analysis to obtain a dimensionless flow equation (Section "Dimensionless Flow Equation"). Both equations are derived based on the parameters shown in Fig. 2.

Dimensional Flow Equation

Using the Bernoulli equation, a system in which the energy is assumed to be conserved is set from the toe on the wave-facing side to the toe on the lee side. Consequently, the Bernoulli equation is adjusted as follows:

$$z_1 + h_1 + \frac{u_1^2}{2g} = z_2 + h_2 + \frac{u_2^2}{2g} + h_L \tag{2}$$

where $z_1 = 0$; $h_1 = P + h$; and h_L is the head loss (m). This equation is rewritten as follows assuming the initial flow velocity and head losses to be expressed by a correction factor α:

$$u_2 = \alpha\sqrt{2g(h_1 - (h_2 + z_2))} \tag{3}$$

Considering the observed prototype's field conditions and practical constraints, this equation is simplified by expressing the overflow velocity entirely in terms of z_2, such that h_2 is assumed to be negligible. Consequently, the overflow velocity can be expressed as the difference between h_1 and z_2, which is independent of the groin height. The overflow velocity increases along the slope until it reaches the leeward water level. As there was no initial lee-side water level during the experiment, a notional lee-side water level was used to extract the flow velocities. This notional water level corresponds to the position at which the water level would have been at bed level. The lee-side water level measured from the crest was expressed as a theoretical freeboard resulting from the lowering in water level as the wave crest of the primary ship-induced wave passes. This dynamic, described by Melling et al. (2021), consists of the following two stages: (1) at first, as the ship-induced wave propagates toward the riverbank, the water level at the groin rises until reaching the wave crest height; and (2) afterward, the water level will withdraw as the wave passes. The previously described theoretical freeboard can also be considered the vertical distance between the groin crest and the level on the groin surface above which the mean velocity is evaluated. Consequently, the dimensional overflow velocity along the lee side of the groin (u) can be expressed in terms of h and R_c as

$$u(h, R_c) = \alpha\sqrt{2g(h + R_c)} \tag{4}$$

Dimensionless Flow Equation

The Buckingham Pi theorem was used to express the overflow velocity along the lee side of the groin in a dimensionless form. This mathematical theorem relates the dimensionality of a physical system to the number of dimensionless groups formed from different independent variables. Therefore, based on a continuous flow over groins, the function f can be determined using the following variables:

$$f(u,\ h,\ R_c,\ g, \mu, \rho_w, \sigma, d_{n50,a}, \theta) \tag{5}$$

The parameters h, ρ_w, and g are selected as the dimensional independent variables because they describe the length, fluid, and flow characteristics. Consequently, six dimensionless groups were obtained, which could be further reduced to two independent

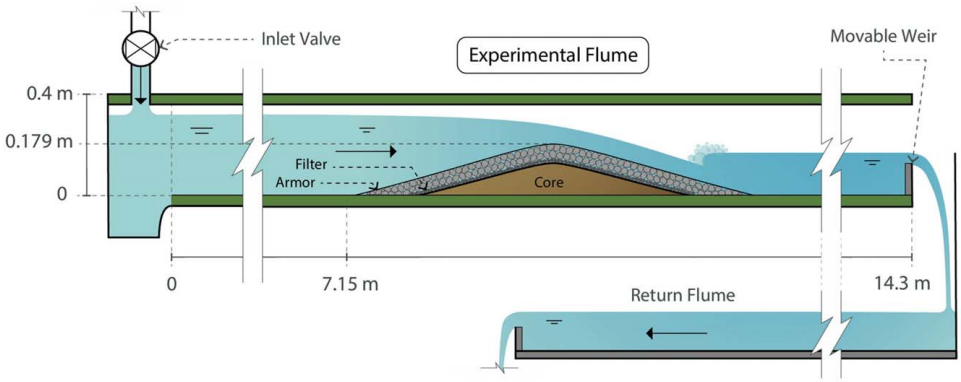

Fig. 1. Cross section of the setup in the flume. For structural details please refer to Fig. 2.

dimensionless groups to express the overflow velocity as

$$\frac{u}{\sqrt{gh}} = f\left(\frac{R_c}{d_{n50,a}}, \theta\right) \tag{6}$$

Prototype Dimensions and Hydraulic Conditions

During the lifetime of the groin in the Lower Elbe Estuary, it was renovated several times (Melling et al. 2021). Therefore, the core material consists of remnants of historical groins that are relatively impermeable. The most recent renovation, forming the study's prototype, consisted of a new armor layer of high-density iron silicate rock ($LM_{5/40}$) with a nominal rock diameter of $d_{n50,a} =$ 0.11–0.23 m and a corresponding rock density of $\rho_s = 3{,}800$ kg/m^3. The new renovation also consisted of changing the slope of the groin from $\theta = 1{:}3$ to $\theta = 1{:}4$, groin width of $W = 19$ m, slope length of $W_s = 8.5$ m, and a crest width of $W_c = 2$ m. The groin also has a height of $P = 2.33$ m with a radius of $R = 3.9$ m.

The BAW conducted a field study to determine the hydraulic conditions in the Lower Elbe Estuary by measuring wave data at the crest of the groin. According to Melling et al. (2021), over 90% of the primary waves were smaller than 0.5 m, and those greater than 1 m were defined as large waves, representing only 1% of the total 1,850 measured primary waves. The maximum primary wave height recorded at the crest was 1.4 m. Hence, these data can be summarized using a dimensionless range of the hydraulic head to groin height as follows:

$$0 < h/P < 0.6 \tag{7}$$

The same study also reported flow velocities at the crest, which were typically <0.5 m/s. Furthermore, approximately 27% of the flow velocities on the wave-facing side exceeded 1 m/s, and frequently reached 2 m/s.

Tested Physical Models and Experiment Flow Conditions

Tested Physical Models

To have a general flow velocity equation, physical models of different θ and $d_{n50,a}$ are tested. All tested models had a wooden core covered with a single sheet of aluminum, a single layer of glued filter layer rock, and two $d_{n50,a}$ thick layers of glued armor. These layers were glued together to maintain the same dimensions throughout the experiments. The inclusion of a filter layer in the physical models was necessary to ensure proper contact between the armor layer and the aluminum sheet covering the wooden core. Furthermore, a length scale of $L_r = 13$ (i.e., the scaling ratio) was used, which was the largest dimension that could fit the flume with the desired hydraulic conditions and would fulfill the scale model criteria. As mentioned in the previous section (i.e., Section "Prototype Dimensions and Hydraulic Conditions"), the prototype armor layer was composed of iron silicate. This material is relatively rare for the construction of rock structures in the Netherlands and is hence unavailable for use in building physical models. A standard rock material such as granite has a density of $\rho_s = 2{,}600$ kg/m^3. An available material with higher density than standard rock is basalt, which has a density of $\rho_s = 2{,}800$ kg/m^3. Because the armor and filter layers are glued in all models, the density of the rock is generally unimportant for scaling. Therefore, the Froude similarity is used to scale the rock sizes of the armor layers made of granite (i.e., standard rock material with relatively smaller density). Furthermore, for the armor layers made of basalt (i.e., rock material with a relatively high density), the Izbash stability equation is used for scaling, which includes the density of the rock and water, rock diameter, and critical flow velocity. Consequently, the effects of differently scaled rock sizes on the flow velocity at the lee side of the model could be assessed.

The following four physical models were therefore built:

Table 1. Dimensions of all tested models with the nominal stone diameters

Parameter	Prototype	Model 1	Model 2	Model 3	Model 4
P (m)	2.33	0.179	0.179	0.179	0.179
W_c (m)	2	0.154	0.154	0.154	0.154
W_s (m)	8.5	0.654	0.654	0.508	0.508
W (m)	19	1.462	1.462	1.170	1.170
θ (−)	1:4	1:4	1:4	1:3	1:3
Armor material	Iron silicate	Basalt	Granite	Basalt	Granite
ρ_s (kg/m^3)	3,800	2,800	2,600	2,800	2,600
$d_{n50,a}$ (m)	0.17	0.019	0.013	0.019	0.013
$d_{n50,f}$ (m)	—	0.010	0.010	0.010	0.010

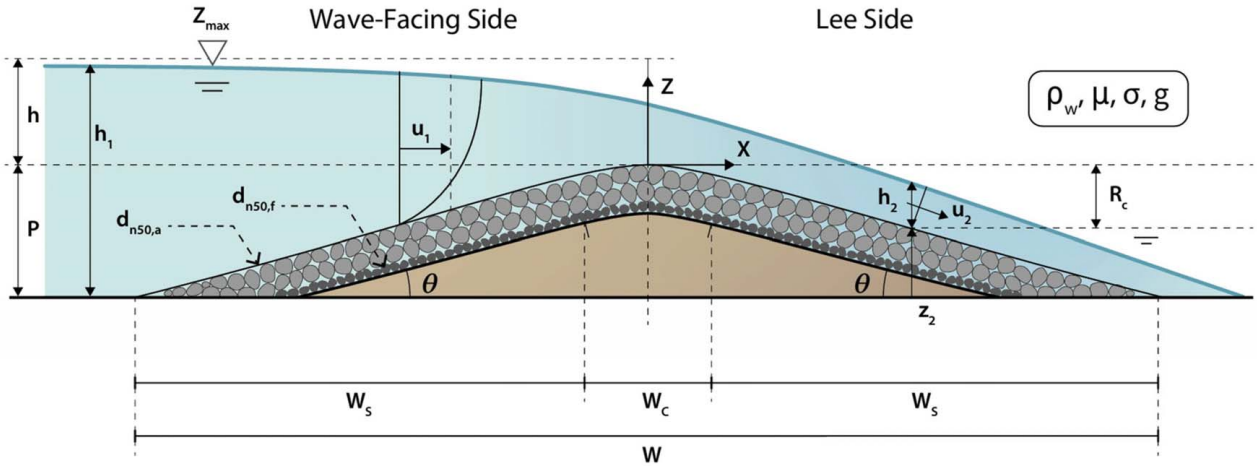

Fig. 2. Schematic representation of the overflow of long-period primary ship-induced waves on the lee side of a groin.

1. **Model 1:** Based on the dimensions of the prototype with a slope of $\theta = 1{:}4$ and fixed armor and filter layers of $d_{n50,f} = 0.019$ and $d_{n50,f} = 0.010$m, respectively.
2. **Model 2:** Based on the dimensions of the prototype with a slope of $\theta = 1{:}4$ and fixed armor and filter layers of $d_{n50,f} = 0.013$ and $d_{n50,f} = 0.010$m, respectively.
3. **Model 3:** Based on the height of the prototype but with a steeper slope of $\theta = 1{:}3$. It also has fixed armor and filter layers of $d_{n50,f} = 0.019$ and $d_{n50,f} = 0.010$m, respectively.
4. **Model 4:** Based on the height of the prototype but with a steeper slope of $\theta = 1{:}3$. It also has fixed armor and filter layers of $d_{n50,f} = 0.013$ and $d_{n50,f} = 0.010$m, respectively.

The dimensions of all tested models are provided in Table 1.

Experiment Flow Conditions

The wave-facing water depth above the crest level was assumed to be equivalent to the hydraulic head, with a range of $0 < h/P < 0.6$. In this experiment, the lower limit of h/P ratio was increased to $h/P = 0.3$, because hydraulic heads (or water levels) that are too low will not meet the physical modeling requirements described by Hughes (1993) and Chanson (2004). To provide a more general flow velocity equation, the upper limit of h/P ratio is increased by 50% to be $h/P = 0.9$ and thus the tested range of h/P ratio was $0.3 < h/P < 0.9$. Five different hydraulic heads were tested, and their corresponding flow velocities on the lee sides of Models 1, 2, 3, and 4 were measured using a PIV system. The details of the PIV measurement technique are provided in Section "PIV Experimental Setup." Three runs (or repetitions) of 20 s each were performed for each hydraulic head to ensure the consistency, accuracy, and reliability of the measurements. Therefore, in case any discrepancies occurred between measurements, the data can be analyzed to determine whether the problem resulted from instrument error, environmental factors, or other variables. As there were four models, 60 individual measurements were performed. The first three hydraulic heads were based on field measurements (prototype), whereas the two additional hydraulic heads account for potentially increased wave heights in the future. A summary of the hydraulic conditions is presented in Table 2.

Table 2. Summary of the hydraulic conditions used to measure the overflow at the lee side of the tested models

Item	Description
Prototype h/P ratio	$0 < h/P < 0.6$
Tested h/P ratio based on the prototype	$0.3 < h/P < 0.6$
Extended h/P ratio	$0.6 < h/P < 0.9$
Model h dimension (cm)	5.4, 8.1, 10.8, 13.5, and 16
Equivalent h dimension for the prototype (cm)	70.2, 105.3, 140.4, 175.5, and 208
Tested models	Models 1, 2, 3, and 4
No. of run (repetitions)	Three runs of 20 s for each model and hydraulic head

PIV Experimental Setup

A planar-PIV setup was used to measure the two-dimensional velocity field on the lee side of the physical models. A typical PIV setup includes a high-speed camera, a high-power light source, tracer particles, and an optical arrangement to convert the light output into a light sheet. The light sheet was pointed at the region of interest. The light source is reflected by the tracer particle with a diameter d_τ and captured by the camera. The corresponding locations can be assigned to particles per frame. The displacement and velocity are obtained by taking two consecutive frames (called a frame pair), recorded at t_0 and $t_0 +$ increment t. Each frame was divided into smaller sections, called interrogation windows, with square dimensions D_I. Moreover, each window is compared with another frame within a frame pair. In each interrogation window within a frame pair, the displacement and velocity vectors were assigned based on the cross-correlation. This procedure yielded an overall two-dimensional velocity field for each frame pair. An illustration of this procedure and a close-up view of the two frames within a frame pair are shown in Fig. 3.

In this study, the PIV setup consisted of a complimentary metal-oxide-semiconductor (CMOS) camera (FLIR Oryx 2,448 × 2,048 pix^2, pixel size $d_\tau = 3.45$ μm) positioned perpendicular to the glass sidewall. The Fujinon TV Lens HF12.5SA-1 was attached to the camera, which has an aperture of F1.8 and a focal length of 12.5 mm. The distance between the camera chip and the LED light sheet was 1 m, providing a maximum field of view of approximately 535 mm × 445 mm in width and height, respectively. The LED light sheet was placed in the center of the flume because, at this location, the flow interaction with side walls is the least. Moreover, the LED light sheet shone from the top onto the armor layer of the models, illuminating 600 mm in length and 6 mm in width. This 600 mm illumination length covers 77 mm in front of the crest top and 523 mm of the lee-side slope of all tested models. The entire setup is covered to block ambient light. The flow was seeded

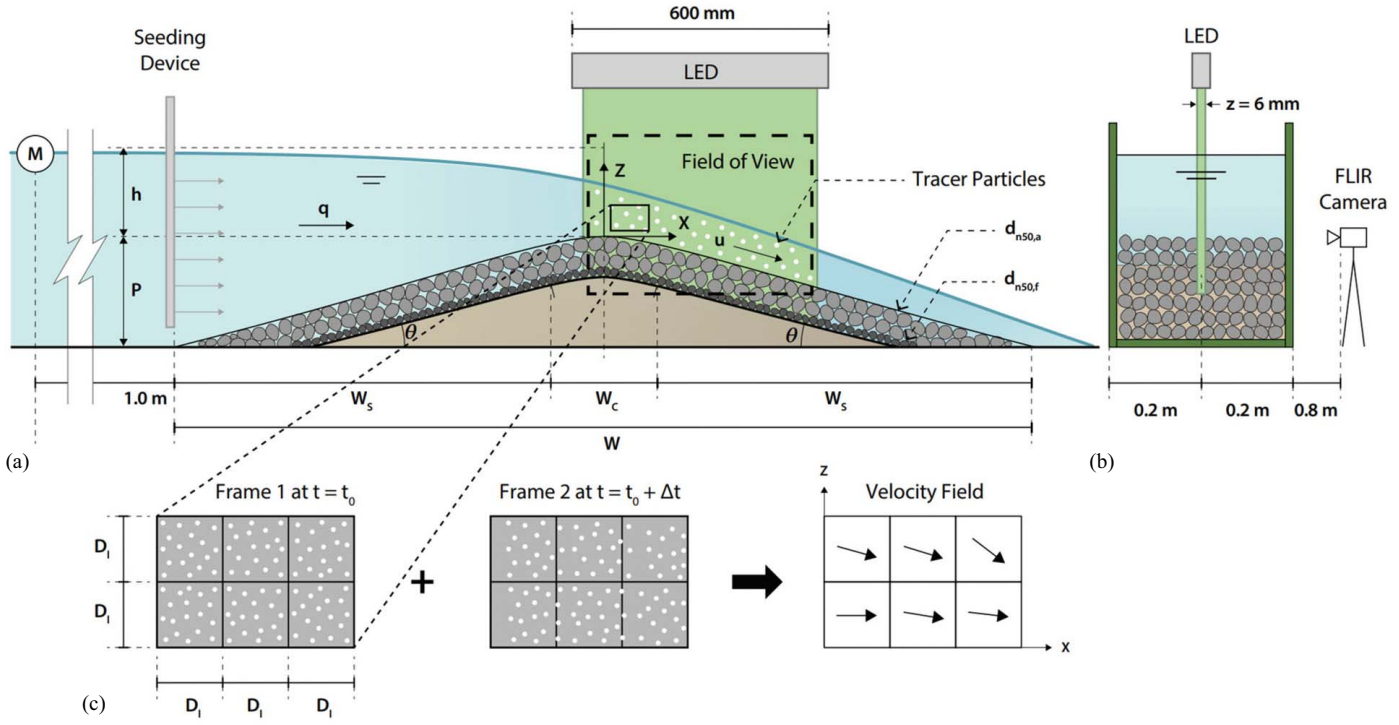

Fig. 3. Illustration of the PIV setup with a corresponding field of view during the overflow experiments: (a) Side view of the physical model with the LED light sheet and the seeding system at the toe of the structure; (b) Front view of the flume with the distances between the LED light source and camera; and (c) Close-up of two frames within a frame pair leading to the velocity field.

with tracer particles Vestosint 1101 ($d_p = 100$ µm and $\rho_p =$ 1,060 kg/m^3). A separate device was designed to inject the tracer particles into the flowing water and is called the seeding device. It consists of a container of water with a concentration of 50 g/L of particles, a mixer, a pump, and an outlet. The device was placed vertically from the top of the flume into the water and directly at the toe of the structure. It injects the particles into the same direction as the flow using 16 horizontal tubes of 19 cm length, 8 mm diameter, and 2 mm outlet diameter. The elements of the PIV setup are listed in Table 3, and the experimental setup is shown in Figs. 3 and 4. The water levels at the wave-facing side were measured by a point needle at 1 m before the toe of the structure and marked by M in Fig. 3. Similarly, the water levels at the crest were measured by a point needle before performing a PIV measurement.

To perform PIV measurements accurately, the PIV settings were selected according to the procedure introduced by Adrian and Westerweel (2011). Hence, to ensure suitable image density, a particle concentration of 50 g/L was selected to have more than 10 tracer particles per interrogation window sized $D_I = 32$ pix (0.007 m) under all tested hydraulic conditions. The camera and LED light sheet were triggered at a frequency of 20 Hz. A single measurement run lasted 20 s, resulting in 400 single frames and, therefore, 200 frame pairs. These frame pairs were processed using the MATLAB (Version R2024b) package PIVLab. A measurement duration of 20 s was determined by calculating the normalized average flow velocity of the different tested hydraulic heads at the crest of the physical model. As shown in Fig. 5 for Model 2, the measured depth-averaged flow velocity (u) is reaching the time-averaged flow velocity (u_{avg}) within 20 s. This graph also shows that the depth- and time-averaged flow velocities are increasing in accuracy as the spread around $u/u_{avg} = 1.0$ becomes smaller. Furthermore, the moving average of the flow velocity approached the average with a deviation of less than 0.5% after 8 s. Hence, to ensure this level of accuracy, the total measurement duration was increased to 20 s per run. To reduce the in-plane pair loss, the time between two frames within a frame pair (i.e., the time between two light pulses or time delay; Δt) was changed per tested hydraulic depth because of the larger traveled distance by the particles at larger hydraulic heads. This distance must be less than 1/4

Table 3. Elements of the PIV setup used during the overflow experiment

Elements of the PIV setup	Name of the product
Pulsed LED line-light	Made in-house (Bakker et al. 2021)
Tracer particles	Vestosint 1101: 100 µm
Camera system	Oryx ORX-10GS-51SM-C
Lens	Fujinon TV Lens HF12.5SA-1 1:1.4/12.5 mm
Data processing	MATLAB package PIVLab (Thielicke 2022; Thielicke and Sonntag 2021)

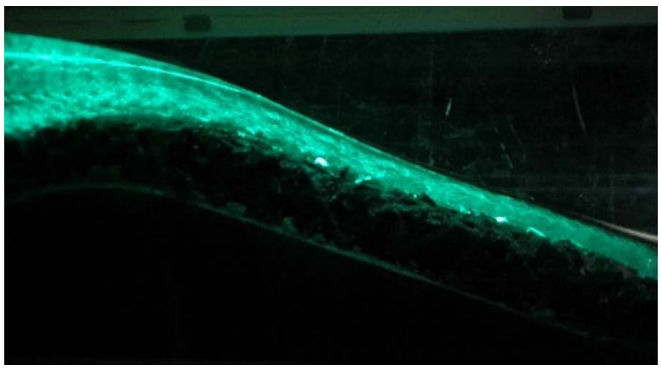

Fig. 4. Flow on crest and downstream slope illuminated by LED light during PIV measurements.

Table 4. Details of the experimental setup of the flow velocities at the lowest position (maximum velocities) and the crest (minimum velocities)

Camera	Properties	Parameter	$h = 8.1$ cm	$h =$ 10.8 cm	$h =$ 13.5 cm	$h = 16$ cm
Oryx ORX-10GS-51S5M-C	Resolution width (pix)	—	2,448	2,448	2,448	2,448
	Resolution height (pix)	—	2,048	2,048	2,048	2,048
	Pixel distance (μm)	d_r	3.45	3.45	3.45	3.45
	Sensor size width (mm)	X_s	8.4	8.4	8.4	8.4
Lens	Sensor size height (mm)	Y_s	7.1	7.1	7.1	7.1
Fujinon TV Lens	Focal length (mm)	f	12.5	12.5	12.5	12.5
HF12.5SA-1						
1:1.4/12.5 mm	f# (−)	f-number	1.8	1.8	1.8	1.8
Light source	Aperture (mm)	D_a	6.94	6.94	6.94	6.94
LED DrewLear VLX2-500	Light wavelength (nm)	λ	530	530	530	530
	Illumination time (μs)	τ_{ill}	100	100	100	100
	Light sheet thickness (mm)	z_0	6	6	6	6
Tracer particles	Focal length (mm)	f_{led}	350	350	350	350
Vestosint 1101	Avg. particle diameter (μm)	d_p	100	100	100	100
	Mass density (kg/m^3)	ρ_p	1,060	1,060	1,060	1,060
	Particle volume (mm^3)	V_p	5.24×10^{-4}	5.24×10^{-4}	5.24×10^{-4}	5.24×10^{-4}
	Added mass particles (g/s)	m_p	0.75	0.75	0.75	0.75
	Stokes number at the lowest position (-)	St_{pl}	9.49×10^{-5}	1.01×10^{-4}	1.07×10^{-4}	1.13×10^{-4}
PIV processing	Stokes number at the crest (-)	St_{p_c}	4.33×10^{-5}	4.99×10^{-5}	5.58×10^{-5}	6.06×10^{-5}
MATLAB package PIVLab	Interrogation window size (pix)	D_i	32	32	32	32
	Overlap (%)	D_0	50	50	50	50
	Trigger frequency (Hz)	f_{acq}	20	20	20	20
Setup dimensions	Time delay (μs)	Δt	1,300	1,100	950	800
	Object distance (m)	z	1	1	1	1
	Min. width of field of view (m)	—	0.535	0.535	0.535	0.535
	Min. height of field of view (m)	—	0.445	0.445	0.445	0.445
Fluid properties	Volume of complete set up light (m^3)	V_{tot}	1.73×10^{-3}	2.31×10^{-3}	2.78×10^{-3}	3.42×10^{-3}
	Mass density (kg/m^3)	ρ_f	998.2	998.2	998.2	998.2
Flow conditions	Kinematic viscosity (m^2/s)	ν_f	1.05×10^{-6}	1.05×10^{-6}	1.05×10^{-6}	1.05×10^{-6}
	Integral in-plane velocity scale at the lowest position (m/s)	u_{0_l}	1.6	1.7	1.8	1.9
	Integral in-plane velocity scale at the crest (m/s)	u_{0_c}	0.73	0.84	0.94	1.02
	Integral out-of-plane velocity scale (m/s)	v_0	0.2	0.2	0.2	0.2
	Integral length scale (m)	l_0	0.55	0.55	0.55	0.55
	Integral time scale at the lowest position (s)	τ_{0l}	0.343	0.323	0.305	0.289
	Integral time scale at the crest (s)	τ_{0c}	0.753	0.655	0.585	0.539
	Reynolds number at the lowest position (−)	$u_{0_l} \times l_0/\nu_f$	8.35×10^5	8.88×10^5	9.40×10^5	9.92×10^5
	Reynolds number at the crest (−)	$u_{0_c} \times l_0/\nu_f$	3.81×10^5	4.39×10^5	4.91×10^5	5.33×10^5

the size of the interrogation window. The illumination time per frame was set at 100 μs to have sufficient light intensity to observe the particles. To reduce the out-of-plane pair loss, the traveled distances of the particles perpendicular to the light sheet must be smaller than 1/4 the width of the sheet. This light sheet was 6 mm wide, which is approximately the same width as that used for the interrogation window of 7 mm. Moreover, the main flow is significantly larger in the parallel direction; therefore, it is presumed that the out-of-plane pair loss rule is satisfied per Adrian and Westerweel (2011). Limited spatial gradients are obtained when the local variation of the image displacement during Δt (i.e., particle displacement within a frame pair) is smaller than the image particle size. During all the experiments, the local variation was equal to or smaller than 2.6 μm, whereas the image particle size was constant at 2.7 μm. Details on the PIV experimental setup and the output requirements for all tested hydraulic heads are provided in Tables 4 and 5.

Notably, as each model was different from the others, a calibration procedure was performed for each model. This procedure included the measurement of a reference point on the model before and after the PIV measurements to ensure that the model and camera were fixed at the same position. A checkerboard of 10 mm × 10 mm squares was used in the calibration by positioning it at a particular location on the model at the center of the light sheet and a filled flume. Consequently, a picture was taken and used to calibrate the velocity measurements using PIVLab.

Flow Velocity Analysis

To analyze the flow velocities, five locations along the lee side were used to extract the flow velocity profiles. The first extraction line (L_c) was positioned at the crest of the models, whereas the other four extraction lines were placed perpendicular to the slope of the lee side ($L_{s1,2,3,4}$), as shown in Fig. 6. At each location, the flow velocity was extracted over the water depth (U). Consequently, a flow velocity profile was obtained for each position perpendicular to the armor layer. The x-coordinates of the extraction lines and corresponding freeboards are listed in Table 6. The depth- and time-averaged velocities (U_{avg}) obtained from these extraction lines were used to determine the overflow velocity equations [Eqs. (4) and (6)].

The captured frames were processed using the MATLAB PIVLab package. All the models were tested with five different

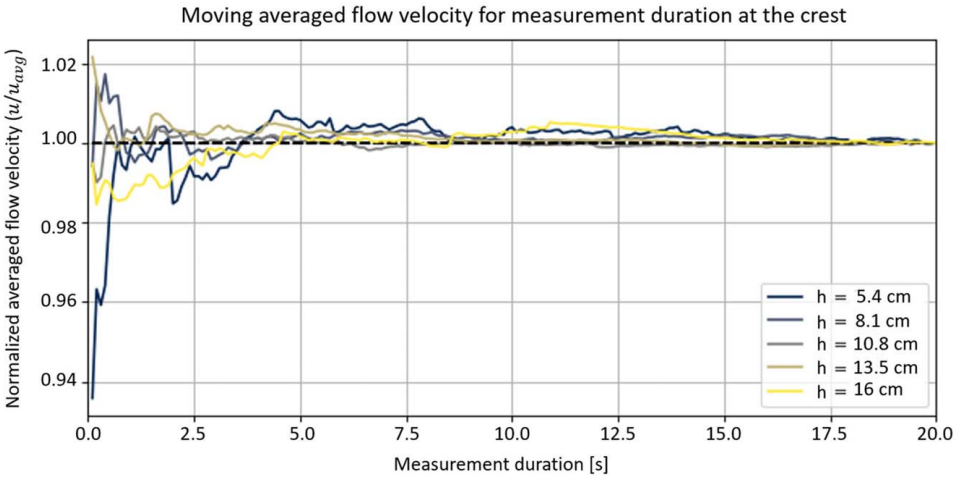

Fig. 5. Normalized average flow velocity of the different tested hydraulic heads at the crest of Model 2.

hydraulic heads. Each head was tested in three runs of 20 s each at a frame rate of 20 Hz, resulting in 400 frames (200 frame pairs). These frames were imported to PIVLab and preprocessed by applying contrast-limited adaptive histogram equalization (CLAHE) and autocontrast filters. The CLAHE filter increases the readability of the image data. Regions with low or high exposure were independently optimized. The CLAHE filter also improves the probability of detecting valid displacement vectors in frames by 4.7% ± 3.2% (Thielicke and Stamhuis 2014). The autocontrast filter automatically calculates the best contrast per frame to improve particle visibility. The discrete Fourier transform (DFT) method was used to calculate the correction matrix in the frequency domain. This method requires 20% of the computational time of the direct cross-correlation (DCC) method (Thielicke and Stamhuis 2014). Therefore, the DFT method was selected in this study because of the large number of experiments performed and captured frames. A disadvantage of the DFT function is the potential increase in the background noise because it uses a fixed interrogation window. To reduce the potential background noise, two passes were used with interrogation window sizes of 32×32 and 64×64 pixels, respectively. Moreover, a Gaussian 2×3 point function was applied to determine the peaks in the correlation matrix. After the analysis, a certain amount of noise was still unavoidable; therefore, a standard deviation of 2 and a local median filter of 3 were applied during postprocessing.

Table 5. PIV output requirements for the flow velocities at the lowest position (maximum velocities) and the crest (minimum velocities)

Component	Parameter	Requirement	$h = 8.1$ cm	$h = 10.8$ cm	$h = 13.5$ cm	$h = 16$ cm
Image dimensions	—	—	—	—	—	—
Image distance (mm)	Y_0	—	12.66	12.66	12.66	12.66
Lateral magnification (-)	M_0	—	1.27×10^{-2}	1.27×10^{-2}	1.27×10^{-2}	1.27×10^{-2}
Field of view width (mm)	x_s	—	667	667	667	667
Field of view height (mm)	y_s	—	558	558	558	558
Field of view depth (mm)	Δ_z	—	44	44	44	44
Image particle	—	—	—	—	—	—
Diffraction limited spot diameter at the lowest position (μm)	d_{s_l}	—	2.4	2.4	2.4	2.4
Diffraction limited spot diameter at the crest (μm)	d_{s_c}	—	2.36	2.36	2.36	2.36
Image particle size (μm)	d_τ	—	2.7	2.7	2.7	2.7
Ratio d_τ/d_r	—	$d_\tau/d_r \approx 1$	0.8	0.8	0.8	0.8
Image particle length at the lowest position (μm)	d_{l_l}	—	2	2.2	2.3	2.4
Image particle length at the crest (μm)	d_{l_c}	—	0.9	1.1	1.2	1.3
Image blur parameter at the lowest position (-)	β_{ib_l}	$\beta_{ib} < 2$	1.8	1.8	1.9	1.9
Image blur parameter at the crest (-)	β_{ib_c}	$\beta_{ib} < 2$	1.4	1.4	1.4	1.5
Particle concentration (#/m^3)	N_S	—	0.08	0.06	0.05	0.04
Processing	—	—	—	—	—	—
Interrogation window image size (mm)	x_{vec}	—	8.7	8.7	8.7	8.7
Vector spacing (mm/vector)	—	—	4.4	4.4	4.4	4.4
PIV design rules	—	—	—	—	—	—
No. of particles per interrogation window at the lowest position	N_{I_l}	$N_I > 10$	36	27	22	18
No. of particles per interrogation window at the crest	N_{I_c}	$N_I > 10$	35	26	22	18
In-plane motion at the lowest position (pix)	X_{p_l}	$X_p < 8$	7.6	6.9	6.3	5.6
In-plane motion at the crest (pix)	X_{p_c}	$X_p < 8$	3.5	3.4	3.3	3
Out-of-plane motion (mm)	$\Delta z_{\max}$	$\Delta z_{\max} < 6$	0.26	0.22	0.19	0.16
Spatial gradient at the lowest position (μm)	Δu_{p_l}	$\Delta u_p < d_\tau$	2.6	2.4	2.2	1.9
Spatial gradient at the crest (μm)	Δu_{p_c}	$\Delta u_p < d_\tau$	1.2	1.2	1.1	1

Table 6. Coordinates of the extraction lines and the corresponding assumed freeboard R_c (m) for each model

	Model 1		Model 2		Model 3		Model 4	
Line	x-coordinates	R_c (m)	x-coordinates	R_c (m)	x-coordinates	R_c (m)	x-coordinates	R_c (m)
L_c	0	0	0	0	0	0	0	0
L_{s1}	0.076	0.005	0.078	0.006	0.064	0.002	0.066	0.001
L_{s2}	0.188	0.03	0.172	0.027	0.162	0.020	0.165	0.022
L_{s3}	0.332	0.075	0.282	0.063	0.274	0.116	0.290	0.067
L_{s4}	0.477	0.119	0.463	0.112	0.445	0.125	0.433	0.119

Results and Discussion

This section discusses the results of overflow velocity measurements obtained using the previously described PIV setup. Section "Flow Velocity Fields and Equations" presents the acquired velocity fields at the crest and lee-side slopes of the groins and the derived dimensional and dimensionless flow velocity equations. In Section "Developed Flow Velocity," the measured overflow velocities are used to verify the applicability of the theoretically developed flow velocity based on the Manning equation.

Flow Velocity Fields and Equations

The flow over the physical models is expected to behave differently because of the different slopes and stone sizes of the armor layers. Fig. 7 shows the sample mean velocity field for 20 s of data for each tested model at a hydraulic head of 10.8 cm. The figure shows 45 mm in front of the crest and 490 mm on the lee-side slope. The flow velocity at the crest was approximately 0.7 m/s, and it accelerated along the slope by up to 2.2 m/s. The corresponding measured water level at the crest of each model was approximately 2/3 of the hydraulic head, which was expected because the flow was in critical condition. After the crest, the flow accelerated and reached the supercritical state ($F_r > 1$). Additionally, it is noted in Fig. 8 that the flow velocity profiles are more uniform at or near the crest (i.e., L_c and L_{s1}; Fig. 6), while they become more logarithmic down the slope (i.e., $L_{s2,3,4}$; Fig. 6). In general, behaviors similar to those presented in Figs. 7 and 8 are noted with the other tested hydraulic heads. These behaviors can be linked to field observations by Melling et al. (2021) in which the damage mainly occurred at the lee side of the prototype, where the maximum overflow velocities existed. Seemann et al. (2023) also found hydraulic heads to strongly influence the intensity of the supercritical state.

The depth- and time-averaged velocity (U_{avg}) profiles at $L_{s1,2,3,4}$ are calculated per run for each tested water level. These velocities were used to determine the dimensional flow equations presented in Eq. (4), where h is the hydraulic head at the crest or wave-facing water depth above the crest level. The bed-level positions of $L_{s1,2,3,4}$ are assumed to be the lee-side water levels, which are expressed in freeboard R_c (i.e., $R_{c,s1,2,3,4}$; Fig. 6 and Table 6).

Fig. 9 shows the measured depth- and time-averaged flow velocities for each tested water level per extraction line. Regression analysis was performed to determine the correction α-factor [Eq. (4)] of each model configuration. These factors are also shown in Fig. 9. The α-factors express the influence of different rock diameters and slopes on the flow velocity. Notably, Models 1–4 have α-factors of 0.78, 0.86, 0.82, and 0.84, respectively. The increase of approximately 10% in the α-factors between Models 1 and 2 can be linked to the decrease in the rock size, possibly causing less friction and turbulence. Conversely, only a slight increase of 2.4% is noted in the α-factors between Models 3 and 4 as the rock size decreases. This implies that for slopes steeper than 1:4, the tested rock sizes are less influential on the α-factor than the slope. However, all the α-factor values are close to each other and could be represented in a single flow equation, and the results are shown in Fig. 10

$$U_{\text{avg}} = 0.81 \times \sqrt{2g(h + R_c)} \tag{8}$$

Eq. (8) expresses a dimensional flow velocity equation for two different slopes and rock sizes in the armor layer with an R^2 value of 0.81 and RMS error (RMSE) of 0.14. To determine the velocities for other slopes and rock sizes, the flow velocities must be expressed using a dimensionless equation, as shown in Eq. (6). A dimensionless equation was constructed by plotting the dimensionless depth- and time-averaged velocity of each measured data point against the slope, nominal stone diameter, and extraction location of each model (i.e., assumed freeboard level). This regression is

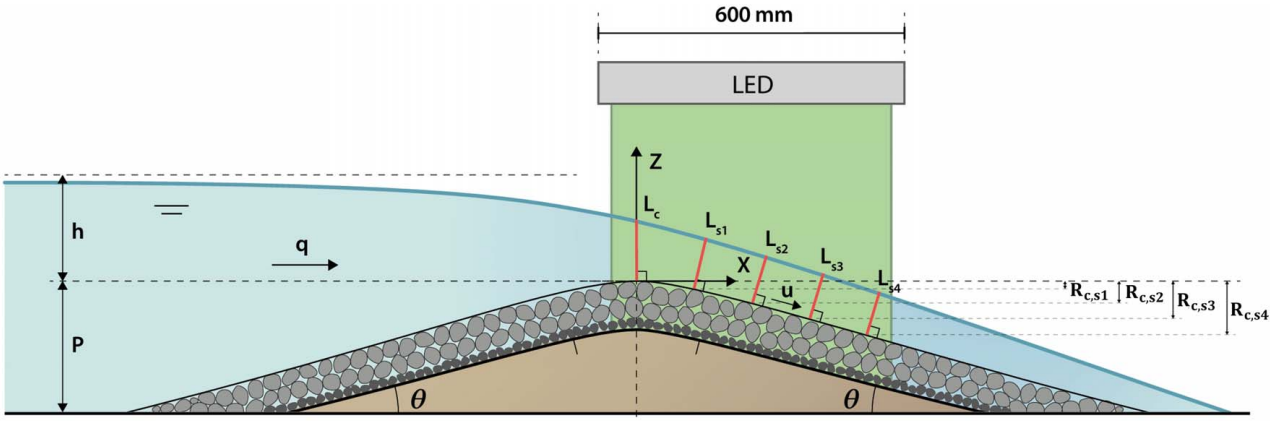

Fig. 6. Side view of the PIV experiment with the location of the extraction lines at the crest (L_c) and the lee side ($L_{s1,2,3,4}$) of the model and the corresponding assumed freeboards ($R_{c,s1,2,3,4}$).

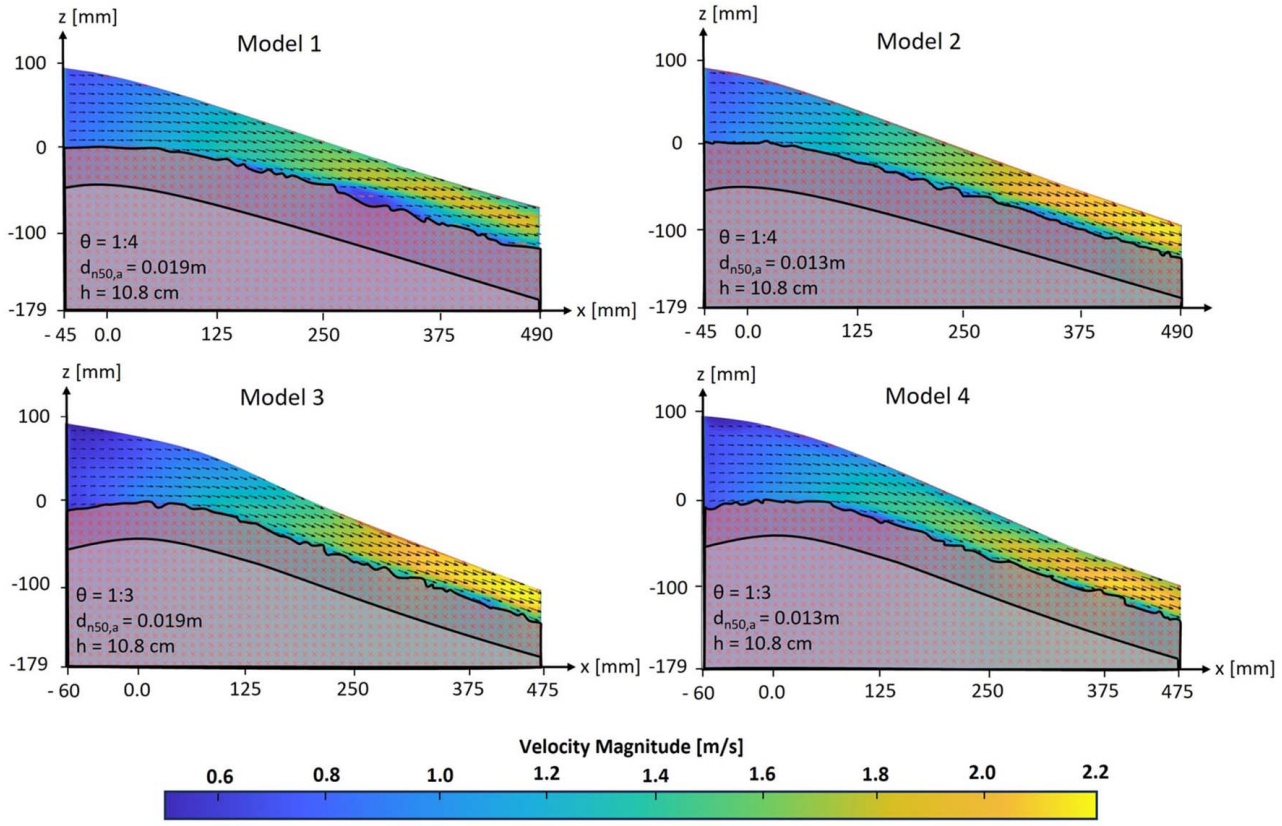

Fig. 7. Flow velocity fields of all tested models at a hydraulic head of 10.8 cm.

shown in Fig. 11 and follows the dimensionless equation:

$$U_{\text{avg}}/\sqrt{gh} = 1.95 - 0.88 \times \exp(-0.51 \times \theta R_c/d_{n50}) \quad (9)$$

Eq. (9) has an R^2 value of 0.89 and an RMSE of 0.08.

Developed Flow Velocity

The measured flow velocities at the crest and lee-side slopes were used to verify the Manning equation for the developed flow [Eq. (1)]. The results of the measured flow velocities per tested water level compared with the theoretically developed flow velocities are presented in Fig. 12. All flow velocities are expressed in terms of the corresponding specific discharge (q). The measurement of the flow velocities started at the crest of the structure, and their values increased as they traveled along the lee-side slope. However, the theoretically developed flow velocity was not reached within the measured region of interest, indicating that the theoretically developed flow velocity was probably too high along the groin slopes for the parameters represented in the model. Furthermore, the developed flow velocities were calculated based on the assumption that no lee-side water level was required to reach the corresponding developed state. Therefore, in the case of a lee-side water level, the flow stops accelerating when it interacts with the lee-side water level, and the flow velocities are thus expected not to reach the theoretical fully developed velocities.

Fig. 12 also presents two standard deviations (σ) around the mean specific discharge ($\bar{q}$). A summary of the measured mean specific discharge, standard deviation, coefficient of variation ($\text{CV} = \sigma/\bar{q}$), and the theoretical fully developed flow velocity are presented in Table 7. Notably, CV at $h = 5.4$ cm was significantly larger than that under the other four tested conditions. This observation could be associated with some difficulties and measurement inaccuracies encountered in the overflow velocities at the lee-side slope with the $h \leq 5.4$ cm (i.e., smaller hydraulic heads) owing to water surface irregularities. The water surface must be flat to allow the LED light sheet to penetrate the water column and be

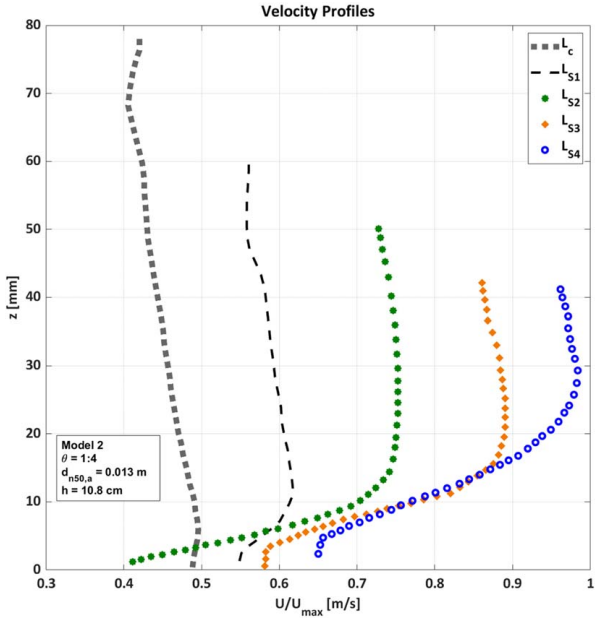

Fig. 8. Flow velocity profiles of Model 2 (which represents the prototype) at a hydraulic head of 10.8 cm along the extraction lines at the crest (L_c) and the lee side ($L_{s1,2,3,4}$) of the model.

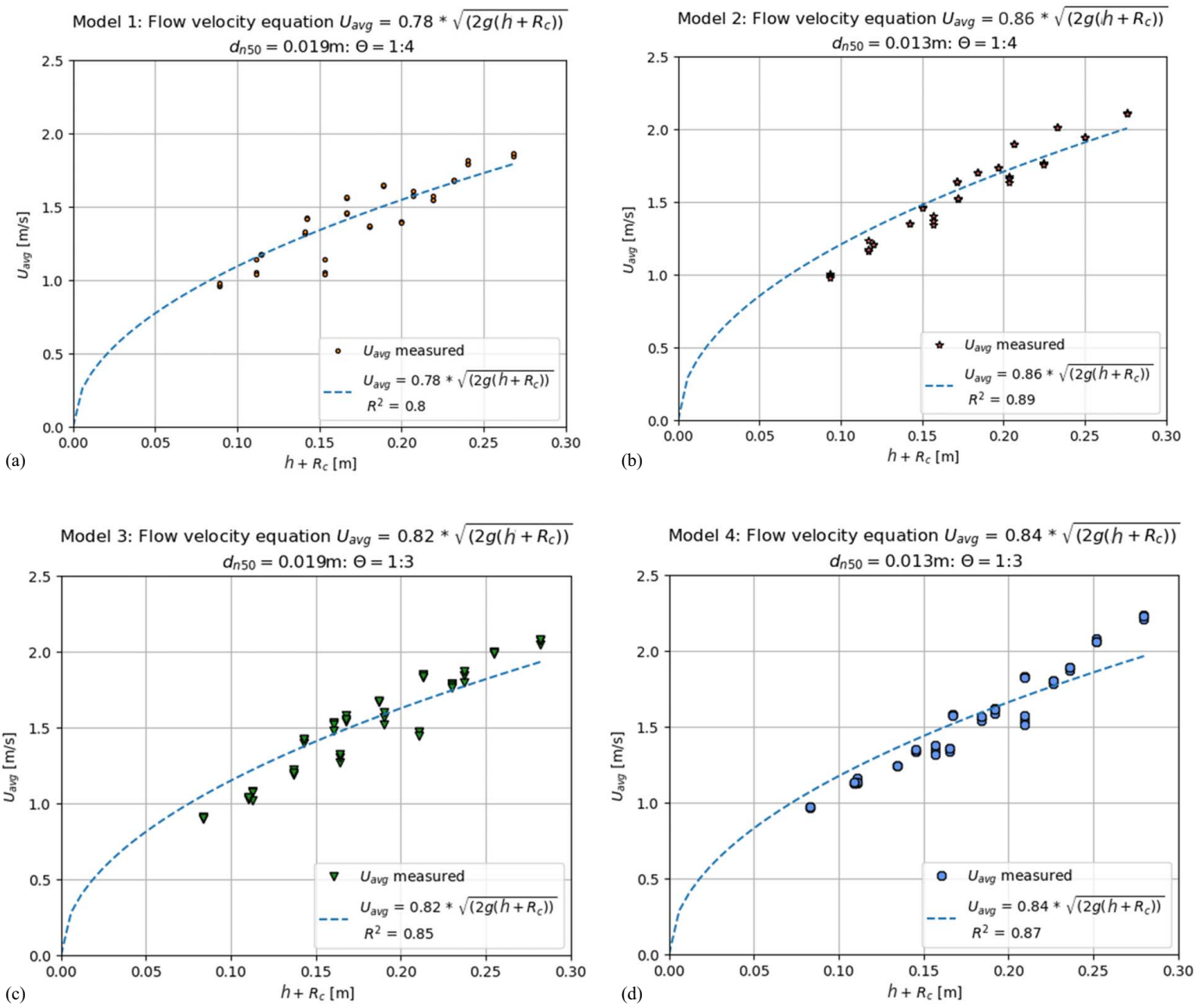

Fig. 9. Depth- and time-averaged flow velocities measured at the extraction lines at the lee side ($L_{s1,2,3,4}$) for each tested model: (a) Model 1; (b) Model 2; (c) Model 3; and (d) Model 4.

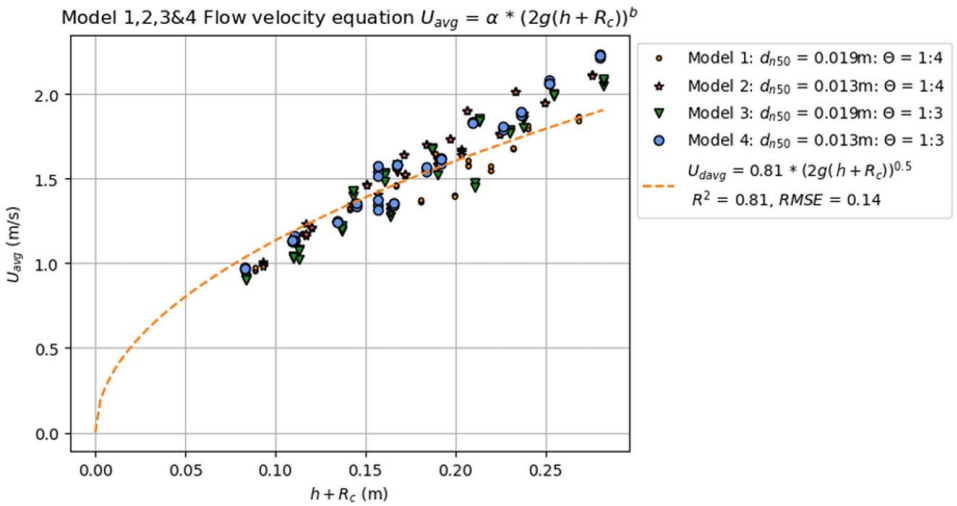

Fig. 10. Optimized flow velocity equation versus flow velocity equation based on the square root for all measurements and tested models.

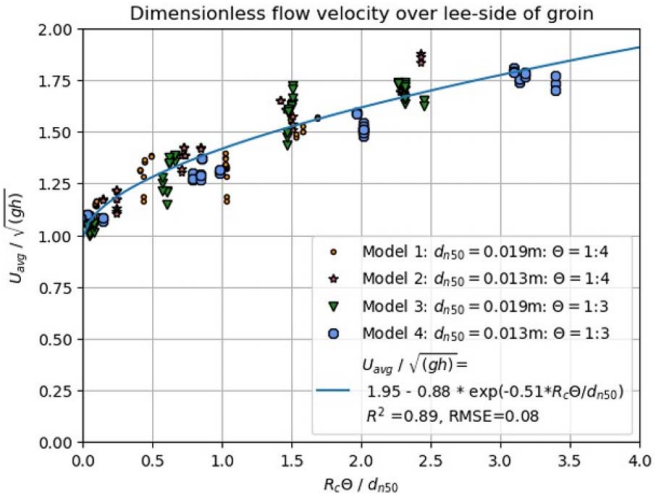

Fig. 11. Dimensionless flow velocity equation in supercritical conditions for upstream water levels above crest level h, assumed lee-side water level R_c, nominal stone diameters d_{n50}, and slopes θ.

captured by the PIV camera. However, when the water surface is not flat (e.g., oscillating), even if the tracer particles cover the entire water depth and the LED light shines through the water, the light can refract from the camera. The analyzed PIV frames showed dark and illuminated parts of the overflowing water on the lee-side slope. This observation was made during all repetitions. Therefore, the $h = 5.4$ cm was discarded for all the models in any of the presented flow equations. Recommendations for overcoming this problem in future studies are presented in the next section.

As the measured flow velocities along the lee-side slope were smaller than the theoretical developed flow velocity, the flow velocities of all models were normalized to their positions on the lee side. This procedure was performed to determine the length required to reach the developed flow velocity, as shown in Fig. 13. All flow velocities were measured within 75% of the leeward slope and reached approximately 80% of the developed flow

Table 7. Measured mean specific discharge, standard deviation, coefficient of variation, and developed flow velocity

h (cm)	$\bar{q}$ (m^2/s)	σ (m^2/s)	CV = $\sigma/\bar{q}$ (%)	u_{dev} (m^2/s)
5.4	0.0136	0.0042	30.7	1.49
8.1	0.0421	0.0012	2.9	1.86
10.6	0.0727	0.0009	1.2	2.18
13.5	0.1070	0.0031	2.9	2.43
16	0.1473	0.0042	2.8	2.58

velocity. Through extrapolation, the developed flow velocities were reached when the length of the lee-side slope was twice the actual length. Therefore, it is concluded that the developed flow equation overestimates the maximum flow velocity by approximately 10%. This information is useful when designing this type of structure.

Conclusions and Recommendations

Main Conclusions of the Study

The aim of this experimental investigation was to develop an equation to express the depth- and time-averaged overflow velocities on the lee side of river groins subjected to different hydraulic heads that can be described by quasi-steady approximation. As a first step toward a design equation, a PIV setup was used to measure the flow velocities at the crest and lee side of four physical models of groins of different slopes ($\theta = 1{:}3$ and 1:4) and stone sizes ($d_{n50,a} = 0.013$ and 0.019 m) in the armor layer under the influence of different hydraulic heads ($h = 5.4$, 8.1, 10.6, 13.5, and 16 cm). The results indicate that the depth- and time-averaged overflow velocities along the lee-side slope accelerated from 0.7 to 2.2 m/s. Consequently, a unified dimensional flow velocity is obtained, as shown in Eq. (8), as a function of h and R_c with an R^2 value of 0.81 and RMSE of 0.14. To make this equation universal and determine the overflow velocities of other slopes and rock sizes, it must be dimensionless. Therefore, Eq. (9) was derived as a function

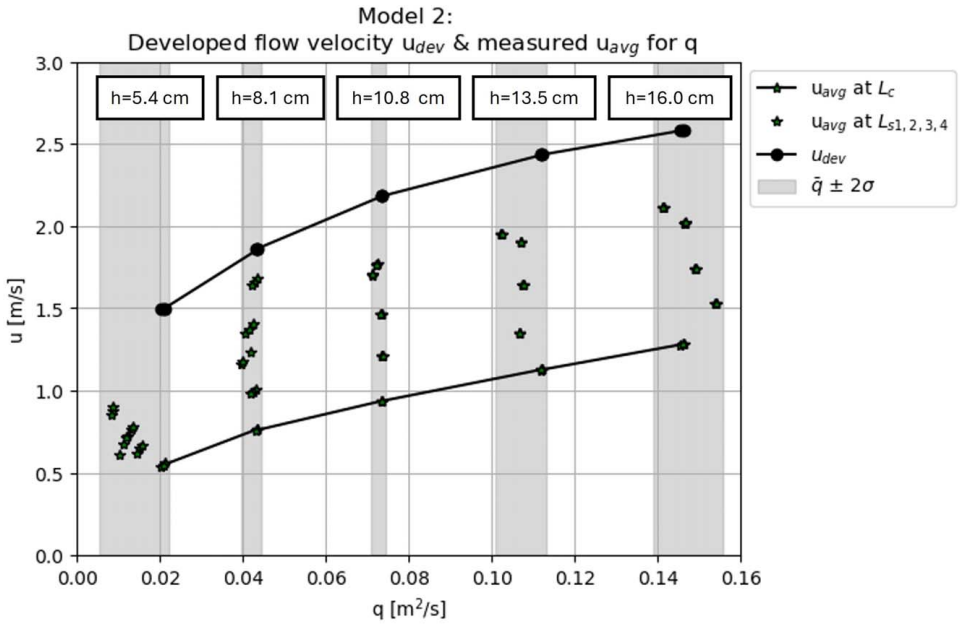

Fig. 12. Measured flow velocities (U_{avg}) at the crest and slope at the lee-side per tested h for Model 2 (which represents the prototype) compared to the corresponding theoretically developed flow velocity (u_{dev}).

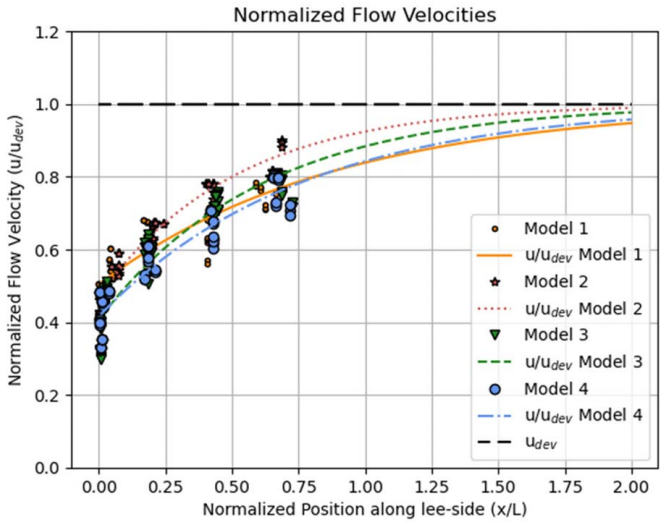

Fig. 13. Normalized flow velocities and the corresponding positions for all models measured along the slope on the lee side.

of h, θ, R_c, and d_{n50} with an R^2 value of 0.89 and RMSE of 0.08. Both Eqs. (8) and (9) can be used under free-flow conditions and for waves that can be described by a quasi-steady approximation in combination with supercritical flow conditions. The theoretically developed flow velocities [Eq. (1)] were also checked for the-r applicability to overflows. At the toe of the lee-side slope, the velocities reached 90% of those of the theoretical developed flow (i.e., the developed flow equation overestimated the maximum flow velocities by approximately 10%). Moreover, the lee-side slope of the structure would need to be twice the overflow velocity to reach a developed state. Therefore, the developed equation in this study can be used by engineers in conjunction with the Seemann et al. (2023) method as a design tool for groins exposed to waves that can be described by the quasi-steady approximation. However, the present study provides a better estimate of the overflow velocity at the lee-side slope as the Seemann et al. (2023) method uses the Manning equation, which turned out to overestimate the flow velocities. Moreover, the study results are valid for all long duration primary waves, groins with slope angles of $\theta = 1{:}3$ to $1{:}4$, nominal rock diameters of $d_{n50,a} = 0.17$–0.23 m, and hydraulic heads of $h = 1$–2.1 m. They are also applicable to structures that are relatively uniform in shape over their length, and to any downstream water level lower than the crest (up to that water level) as the flow is supercritical. In situations where the influence of the structure's size is limited, the study results are expected to be valid even outside these ranges.

Limitations and Recommendations for Future Studies

Based on the knowledge gained from this experimental investigation, recommendations are provided for further improvement and future studies. First, the flow velocities were measured without an initial lee-side water level, resulting in supercritical free-flow conditions and upper limits of the flow velocities. Although this is a safe approach when the derived equations are used as a design tool, the prototype is more likely to be in a subcritical condition because of a water level at the lee side of the structure. Hence, repeating this experimental investigation with the initial water level on the lee side of the test models to represent the more typically occurring subcritical overflow velocities caused by long-period primary ship-induced waves would be beneficial. However, a different PIV setup must be adopted because the existence of an initial water level is expected to cause irregularities in the water surface (i.e., nonflat water surface conditions) at the lee side. Consequently, the overflow velocities could be measured by placing an LED light closer to the flume wall. This approach may still cause unwanted friction between the overflow and flume wall, slightly reducing the velocities. Second, it would be beneficial to repeat the experimental investigation with more slopes and rock sizes to increase the application range of the derived equation to express the overflow velocities on the lee-side slope of river groins. Third, using the present PIV setup with a length scale of $L_r = 13$, which is the largest possible dimension that could fit the models into the flume, the overflow velocities with $h \leq 5.4$ cm could not be measured owing to water level irregularities. This could be solved either by using larger physical models in a larger flume or the same-sized models ($L_r = 13$) but with placing the LED light closer to the flume wall. Fourth, tracer particles were injected at the toe of the structure on the wave-facing side. The seeded water then flowed into the central laboratory basin. Because the tracer particles have a density close to that of water, they would settle slowly in the basin and could contaminate the water of other experimental flumes in the laboratory. Therefore, we attempted to minimize the number of tracing particles used in the experiment by placing the seeding device close to the structure. This approach led to a smaller spread of the tracing particles over the width of the flume and, hence, the need for smaller quantities of particles. However, because of this approach, once every several seconds, the particles were not fully mixed throughout the width of the flume, and a group of highly concentrated particles occurred. Therefore, the PIV software was unable to analyze these groups, and the flow velocities were interpolated. However, these conditions were not expected to influence the depth- and time-averaged flow velocities significantly. To prevent this problem, in future studies, the flume could be disconnected from the central basin, a closed pump system could be created, and better-mixed particles could be added. All these measures could result in an even distribution of particles throughout the entire water column. Consequently, the occurrence of grouped particles is expected to be significantly reduced, leading to more accurate measurements. Additionally, this study focused on the depth- and time-averaged overflow velocities along the lee-side slope, which can be extended in the future to include a detailed analysis of turbulence and shear stresses near the slope surface. Further investigation is also needed to study the effects of ship waves on pore pressures and their influence on slope and armor stability. Finally, the theoretically based overflow equations of Seemann et al. (2023) can be validated using the laboratory measurements obtained in the present study, which would contribute to a broader application of both studies.

Data Availability Statement

Data that support the findings of this study are available from the corresponding author upon reasonable request.

Acknowledgments

The authors thank Wout Bakker from Deltares, who developed the PIV setup used during the experiment and provided guidance and support. The authors sincerely appreciate the support of the staff of the Hydraulic Engineering Laboratory at the Delft University of Technology, Pieter van der Gaag, Chantal Willems, Frank Kalkman, Arie van der Vlies, and Arno Doorn, who assisted in

coordinating the experimental activities in the laboratory and provided technical support.

Notation

The following symbols are used in this paper:

$d_{n50,a}$ = nominal rock diameter of armor layer (m);
$d_{n50,f}$ = nominal rock diameter of filter layer (m);
g = gravitational acceleration (m/s^2);
h = wave-facing water depth above the crest level (assumed to be equivalent to the hydraulic head) (m);
h_1 = wave-facing water depth; $h_1 = P + h$ (m);
h_2 = lee-side water depth (m);
P = groin height (m);
R_c = vertical distance between groin crest and level on the groin surface above which the mean velocity is evaluated (m);
u_1 = initial flow velocity (m/s);
u_2 = flow velocity at the lee side; it is determined at the position where the theoretical lee-side freeboard interacts with the armor layer (m/s);
$z_{\max}$ = maximum water level above the crest level (m);
z_1 = wave-facing bed level; $z_1 = 0$ (m);
z_2 = lee-side bed level (m);
θ = slope (−);
μ = dynamic viscosity of water (kg/m^2/s);
ρ_w = water density (kg/m^3); and
σ = surface tension (N/m^2).

References

Abt, S., J. Ruff, R. Wittler, and D. LaGrone. 1987. "Gradation and layer thickness effects on riprap." In *Proc. National Conference on Hydraulic Engineering*, 564–575. Reston, VA: ASCE.

Adrian, R., and J. Westerweel. 2011. *Particle image velocimetry*. Cambridge, UK: Cambridge University Press.

Ahmad, H., M. Hasan, and N. Tanaka. 2010. "Analysis of flow around impermeable groynes on one side of symmetrical compound channel: An experimental study." *Water Sci. Eng.* 3 (1): 56–66. https://doi.org/10.3882/j.issn.1674-2370.2010.01.006.

Atkins, M. D. 2016. "Velocity field measurement using particle image velocimetry (PIV)." In *Application of thermo-fluidic measurement techniques*, edited by T. Kim, T. Lu, and S. J. Song, 125–166. New York: Butterworth-Heinemann.

Bakker, W., B. Hofland, E. De Almeida, G. Oldenziel, and E. F. J. Overmars. 2021. "Pulsed LED line light for large-scale PIV—Development and use in wave load measurements." *Meas. Sci. Technol.* 32 (11): 115205. https://doi.org/10.1088/1361-6501/ac17ce.

BAW (Bundesanstalt für Wasserbau). 2010. *Bemessung der strombauwerke in der außenweser unter berücksichtigung von schiffswellenbelastungen (baw-gutachten, a39550210120)*. Hamburg, Germany: BAW.

Bertram, V. 2012. *Practical ship hydrodynamics.* Burlington, MA: Butterworth-Heinemann.

Bhowmik, N. G., M. Demissie, and S. Osakada. 1981. *Waves and drawdown generated by river traffic on the Illinois and Mississippi rivers*. ISWS Contract Rep. CR 271. Waltham, MA: Illinois State Water Survey.

Biabani, R., F. Salmasi, M. Nouri, and J. Abraham. 2022. "Flow over embankment gabion weirs in free flow conditions." *J. Hydro-environ. Res.* 44: 65–76. https://doi.org/10.1016/j.jher.2022.08.001.

Chanson, H. 2004. *Hydraulics of open channel flow*. Burlington, MA: Butterworth-Heinemann.

Cheng, X., and J. Gulliver. 2011. "Velocity profile for developing flow over stepped spillway." *AIP Conf. Proc.* 1376 (1): 343–350. https://doi.org/10.1063/1.3651914.

Fritz, H. M., and W. H. Hager. 1998. "Hydraulics of embankment weirs." *J. Hydraul. Eng.* 124 (9): 963–971. https://doi.org/10.1061/(ASCE)0733-9429(1998)124:9(963).

Hughes, S. A. 1993. *Physical models and laboratory techniques in coastal engineering*. Singapore: World Scientific.

Keulegan, G. H., and L. H. Carpenter. 1958. "Forces on cylinders and plates in an oscillating fluid." *J. Res. Nat. Bur. Stand.* 60 (5): 423–440. https://doi.org/10.6028/jres.060.043.

Kindsvater, C. 1964. *Discharge characteristics of embankment shaped weirs*. USGS Water Supply Paper 1617-A. Washington, DC: U.S. Government Printing Office.

Malik, S., and S. Pal. 2019. "Is the construction of groynes accelerating the degradation of channel morphology and paved the way for human encroachment in the Bengal basin?" *Adv. Space Res.* 64 (8): 1549–1576. https://doi.org/10.1016/j.asr.2019.07.024.

Melling, G., H. Jansch, B. Kondziella, K. Uliczka, and B. Gätje. 2021. *Evaluation of optimised groyne designs in response to long-period ship wave loads at Juelssand in the Lower Elbe Estuary*. Karlsruhe: Bundesanstalt für Wasserbau.

Poleni, J. 1717. *De motu aquae mixto libri duo*. Padova: Typis Iosephi Comini.

Prasad, S. K., K. P. Indulekna, and K. Balan. 2016. "Analysis of groyne placement on minimising river bank erosion." *Procedia Technol.* 24: 47–53. https://doi.org/10.1016/j.protcy.2016.05.008.

Seemann, A., G. Melling, H. Jansch, and B. Kondziella. 2023. "A design method for rock groynes exposed to overtopping from long-period ship wave loads." *J. Coastal Hydraul. Struct.* 3: 29. https://doi.org/10.59490/jchs.2023.0029.

Thielicke, W. 2022. "Pulse-length induced motion blur in PIV particle images: To be avoided at any cost?" In *Proc., Fachtagung Experimentelle Strömungsmechanik*. Ilmenau, Germany: German Association for Laser Anemometry (GALA).

Thielicke, W., and R. Sonntag. 2021. "Particle image velocimetry for MATLAB: Accuracy and enhanced algorithms in PIVlab." *J. Open Res. Software* 9 (1): 12. https://doi.org/10.5334%2Fjors.334.

Thielicke, W., and E. Stamhuis. 2014. "PIVlab—Towards user-friendly, affordable, and accurate digital particle image velocimetry in MATLAB." *J. Open Res. Software* 2 (1): e30. https://doi.org/10.5334/jors.bl.

Uijttewaal, W. S. 2005. "Effects of groyne layout on the flow in groyne fields: Laboratory experiments." *J. Hydraul. Eng.* 131 (9): 782–791. https://doi.org/10.1061/(ASCE)0733-9429(2005)131:9(782).

van Steijn, P. W., M. J. Wu, and Y. Broekema. 2023. "Towards a better understanding of loose rock scour protection stability around monopile foundations". In *Proc., 11th Int. Conf. on Scour and Erosion (ICSE-11)*. London, UK: Society for Soil Mechanics and Geotechnical Engineering (ISSMGE).

WSABhv. 2021. *Strombaulicher bericht zur bauwerksunterhaltung und zum ufersicherungs—Konzept am niedersächischen ufer*. Cuxhaven, Germany: WSA Cuxhaven.

WSACux. 2009. *Strombaulicher bericht über den derzeitigen stand der bauwerksunterhaltung an den buhnen und leitwerken in der außenweser*. Bremerhaven, Germany: WSA Bremerhaven.

Xiang, K., Z. Yang, S. Wu, W. Goa, and D. Li. 2020. "Flow hydrodynamics of the mixing layer in consecutive vegetated groyne fields." *Phys. Fluids* 32 (6): 065110. https://doi.org/10.1063/5.0006317.